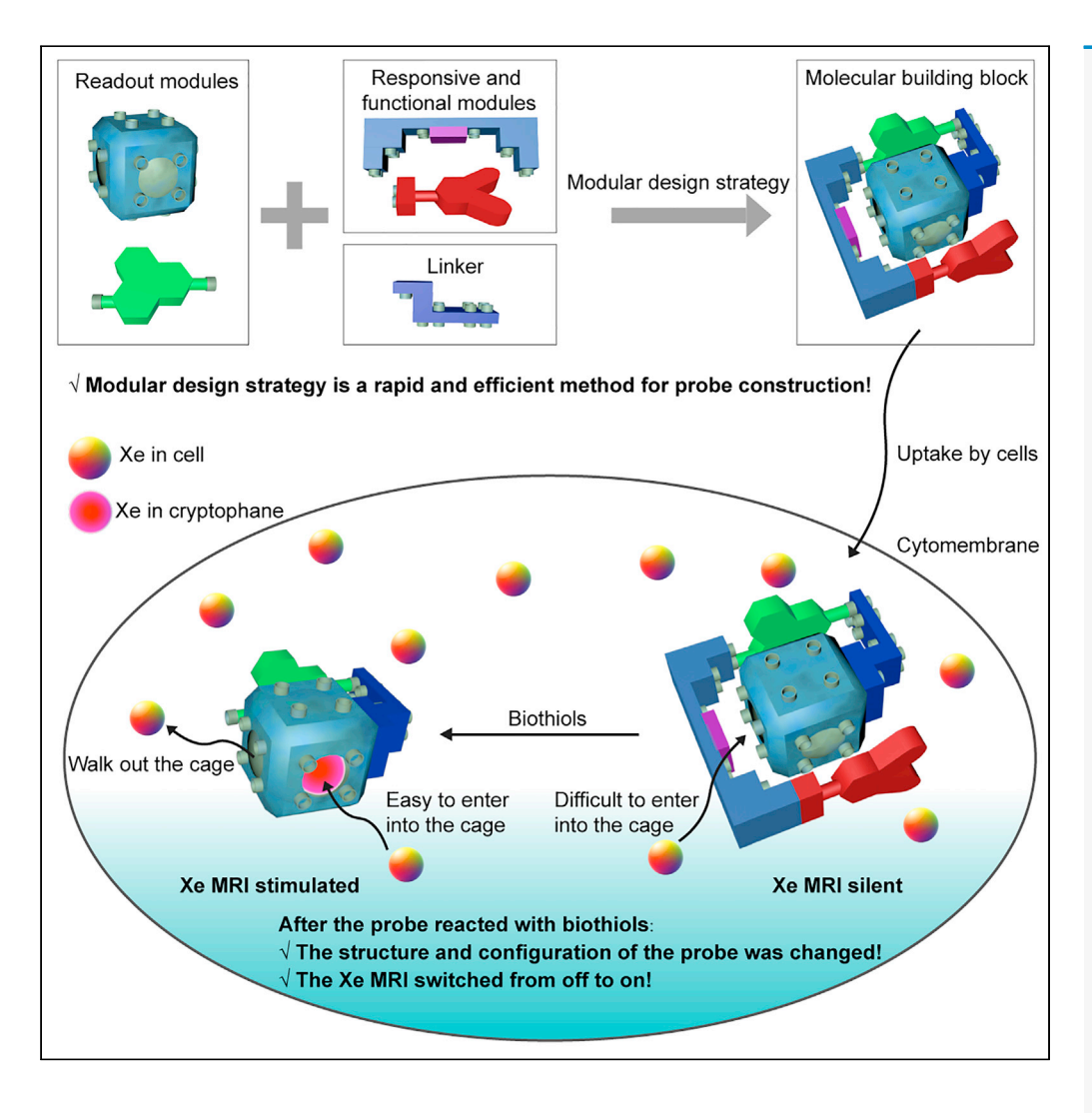




Article

Ultrasensitive molecular building block for biothiol NMR detection at picomolar concentrations



Qingbin Zeng, Qianni Guo, Yaping Yuan, ..., Xin Lou, Louis-S. Bouchard, Xin Zhou

xinzhou@wipm.ac.cn

Highlights

Provide a flexible and efficient strategy for probe construction

The probe shows high NMR detection sensitivity for biothiols

Realize biothiols imaging in live cells by ¹²⁹Xe MRI

Zeng et al., iScience 24, 103515 December 17, 2021 © 2021 The Author(s). https://doi.org/10.1016/ j.isci.2021.103515



iScience



Article

Ultrasensitive molecular building block for biothiol NMR detection at picomolar concentrations

Qingbin Zeng,^{1,2} Qianni Guo,^{1,2} Yaping Yuan,^{1,2} Baolong Wang,¹ Meiju Sui,^{1,2} Xin Lou,³ Louis-S. Bouchard,⁴ and Xin Zhou^{1,2,5,*}

SUMMARY

Magnetic resonance imaging (MRI) provides structural and functional information, but it did not probe chemistry. Chemical information could help improve specificity of detection. Herein, we introduce a general method based on a modular design to construct a molecular building block Xe probe to help image intracellular biothiols (glutathione (GSH), cysteine (Cys) and homocysteine (Hcy)), the abnormal content of which is related to various diseases. This molecular building block possesses a high signal-to-noise ratio and no background signal effects. Its detection threshold was 100 pM, which enabled detection of intracellular biothiols in live cells. The construction strategy can be easily extended to the detection of any other biomolecule or biomarker. This modular design strategy promotes efficiency of development of low-cost multifunctional probes that can be combined with other readout parameters, such as optical readouts, to complement ¹²⁹Xe MRI to usher in new capabilities for molecular imaging.

INTRODUCTION

A well-known application of hyperpolarized ¹²⁹Xe magnetic resonance imaging (MRI) is to simultaneously depict both the structure and function of the respiratory system in a single scan (Li et al., 2016a, 2016b, 2018, 2021; Qing et al., 2014; Xiao et al., 2018; Xie et al., 2019). We have developed a methodology to visualize and quantify a damaged lung's gas exchange function in COVID-19 patients using ¹²⁹Xe MRI during the onset of the pandemic in Wuhan. To compare with the computed tomography (CT) images, we found that the structure of discharged patients' lung is normal in CT images, but the lung's gas exchange function visualized by ¹²⁹Xe gas MRI is abnormal (Li et al., 2021). However, our method of ¹²⁹Xe NMR detection lacks specificity in the sense that it is a structural-functional readout that provides no information about underlying chemical processes. Increased specificity may help improve diagnostic capabilities. Hyperpolarized ¹²⁹Xe probes that result in specific molecular imaging have been considered (Spence et al., 2001). The usefulness of ¹²⁹Xe signals stems from a potential 100,000-fold enhancement through hyperpolarization (Zeng et al., 2020a), enabling its detection at ultralow concentrations. Also, the extremely high sensitivity of the ¹²⁹Xe atom to its local chemical environment (Schröder, 2013) due to its large polarizable electronic cloud confers it the potential to distinguish different molecules or biomarkers (Palaniappan et al., 2014; Taratula and Dmochowski, 2010). This enhanced detection and chemical sensitivity may be leveraged for the design and construction of various ¹²⁹Xe-based MRI probes for multiplexed molecular imaging (Kunth et al., 2012).

The development of ¹²⁹Xe-based probes has greatly benefited from the application of Hyper-CEST methods (Schröder et al., 2006). Hyper-CEST is a signal amplification technique that combines the advantages of hyper-polarized ¹²⁹Xe with chemical exchange saturation transfer (CEST). Primarily, this technique improves the detection sensitivity of ¹²⁹Xe probe MRI and allows the detection of ultralow concentrations of ¹²⁹Xe probe (Meldrum et al., 2010; Riggle et al., 2015; Rose et al., 2014). The other advantage of CEST is that the contrast mechanism can be switched on and off, as a way to minimize false positive outcomes. For Hyper-CEST, the signal is generated from the interaction between Xe and Xe host molecules, such as cryptophane-A (Schröder et al., 2006), cucurbit[6]uril (Kunth et al., 2015), protein (Wang et al., 2016), gas vesicles (Shapiro et al., 2014), pillararene (Adiri et al., 2013), nanoemulsions (Stevens et al., 2013), metal-organic capsules (Roukala et al., 2015; Du et al., 2020), and metal-organic frameworks (Yang et al., 2021; Zeng et al., 2020a). These host

¹Key Laboratory of Magnetic Resonance in Biological Systems, State Key Laboratory of Magnetic Resonance and Atomic and Molecular Physics, National Center for Magnetic Resonance in Wuhan, Wuhan Institute of Physics and Mathematics, Innovation Academy for Precision Measurement Science and Technology, Chinese Academy of Sciences-Wuhan National Laboratory for Optoelectronics, Wuhan 430071, P. R. China

²University of Chinese Academy of Sciences, Beijing 100049, P. R. China

³Department of Radiology, Chinese PLA General Hospital, Beijing 100853, P. R. China

⁴California Nano Systems Institute, Jonsson Comprehensive Cancer Center, The Molecular Biology Institute, Departments of Chemistry and Biochemistry and of Bioengineering, University of California, Los Angeles 90095, USA

51 ead contact

*Correspondence: xinzhou@wipm.ac.cn

https://doi.org/10.1016/j.isci. 2021.103515







molecules bind with Xe transiently and generate a characteristic ¹²⁹Xe chemical shift that is used to help localize the signal in the tissue of interest. The host molecules in the sample can be easily detected in the CEST experiment by saturation of the characteristic resonance frequency. In this manner, ¹²⁹Xe and the host molecule together act as MRI reporters, and the different molecular probes and biomarkers can be detected and spatially resolved through ¹²⁹Xe MRI within the same scan. In recent years, a number of studies have described the development of ¹²⁹Xe-based probes for biotarget detection or multimodal imaging (Chambers et al., 2009; Gomes et al., 2016; Kotera et al., 2015; Roy et al., 2007; Seward et al., 2011; Schlundt et al., 2009; Schnurr et al., 2015; Wei et al., 2006; Witte et al., 2015; Yang et al., 2017; Zeng et al., 2017, 2020b; Zhang et al., 2018, 2020). However, only a few studies have accomplished biotargeting and/or biomolecular imaging in live cells with ¹²⁹Xe MRI (Rose et al., 2014; Witte et al., 2015; Yang et al., 2017; Zhang et al., 2018). Consequently, questions remain as to how to rapidly develop low-cost probes for imaging of different biomolecules in live cells with MRI.

In this study we introduce a modular design construct, the molecular building block, for biomolecular imaging via 129Xe MRI in live cells with no background signal and a remarkably low detection threshold of 100 pM. In order to make the reader deeper understanding the Xe based probe construction strategy, we use the word building block to describe the Xe based probes' construction. The modular design strategy offers several advantages, such as fast and easy extension toward the detection of any other biomolecule or biomarker; versatility, convenience, and flexibility of different probe construction; and low cost of new probe development. Herein we chose biothiol specific detection as an example application for chemical imaging by entrapped hyperpolarized ¹²⁹Xe. Biothiols, such as cysteine (Cys), glutathione (GSH) and homocysteine (Hcy), play vital roles in cellular metabolism. Abnormal biothiol levels in cells are directly correlated to various diseases including cancer, Parkinson's disease, Alzheimer's disease and cardiovascular disease, etc (Lee et al., 2013; Niu et al., 2015; Zhang et al., 2004). Thus, it is critically important to image biothiols in living systems. In our previous study, biothiols were detected in live cells by ¹²⁹Xe nuclear magnetic resonance (NMR) (Zeng et al., 2017). However, due to the ¹²⁹Xe NMR signal (intensity and chemical shift) difference was too small before and after reacted with biothiols, the biothiol MRI in live cells was not achieved. Here, we present a stimulative ¹²⁹Xe MRI "molecular building block", named Molego 1, which is an off-on probe possessed high signal-to-noise ratio. While Molego 1 reacts with biothiols, the entrapped ¹²⁹Xe NMR signal turns from off to on, capable of achieving biothiol ¹²⁹Xe MRI detection in live cells. The Molego 1 combining four functional modules (Figure 1): (1) cryptophane-A, a Xe host molecule, as a ¹²⁹Xe MRI reporter; (2) naphthalimide, a fluorescent molecule, as a fluorescence reporter; (3) disulfide bond linkage, as a biothiol reaction module; and (4) chlorambucil (CRB), a Food Drug and Administration (FDA)-approved anticancer agent, for chemotherapy. These four modules were integrated together as "Lego" building blocks, and the fluorescent module and anticancer agent could be replaced by other molecules, using naphthalimide and CRB as examples in this study. This probe exhibited a high signal-to-noise ratio for NMR detection, even in a complex environment. Molego 1 was no longer dependent on changes in the chemical shift intensity, a result that was different from our previous study (Zeng et al., 2017).

RESULTS AND DISCUSSION

Hyperpolarized ¹²⁹Xe NMR/MRI studies

Molego 1 was prepared using the synthetic route shown in Scheme S1. The chemical structures of all compounds were characterized by 1H NMR, ^{13}C NMR and high-resolution mass spectrometry (HR-MS). Due to the water solubility of Molego 1 is not very good, we use DMSO to increase the solubility of it in PBS buffer. To consider the solubility and Xe exchange rate, we added 50% DMSO into PBS to dissolve the Molego 1. We found that the solubility of 1 in PBS buffer (including 50% DMSO) was $\sim\!16~\mu\text{M}$ (Figure S1). Then, the ^{129}Xe NMR properties of 1 were investigated. After Molego 1 was dissolved in PBS buffer (including 50% DMSO), only a single ^{129}Xe NMR resonance could be observed, namely, the resonance originating from dissolved ^{129}Xe in solution (at 235.96 ppm) (Figure S2A). While Molego 1 reacted with GSH, a weak ^{129}Xe NMR signal appeared at 71.89 ppm (Figure S2B), which is the resonance of the entrapped ^{129}Xe in the cryptophane cage. At the same time, the ^{129}Xe NMR spectrum of cryptophane-A mono acid (25 μM) in PBS buffer (including 50% DMSO) was also obtained, two ^{129}Xe NMR resonance could be observed, and the strong signal near 70 ppm was the NMR resonance of ^{129}Xe in the cryptophane cage (Figure S3). Based on these results, we conclude that the entrapped ^{129}Xe NMR signal was caused by the structure and configuration of Molego 1, but not caused by aggregation.



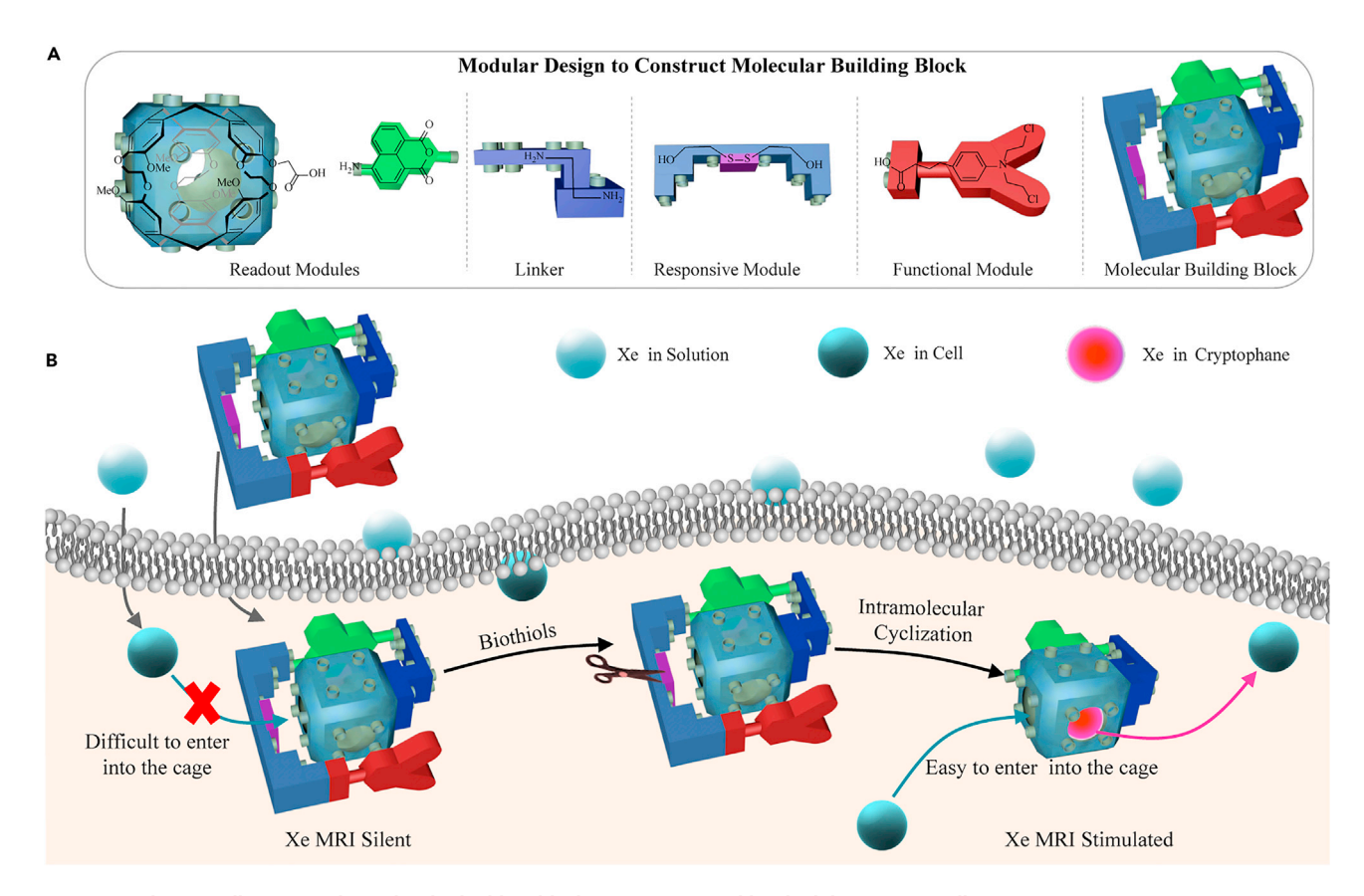


Figure 1. Schematic illustrating the molecular building block construction and biothiol detection in cells

(A) Illustration of the modular design for molecular building block.

(B) Biothiol detection in live cells. After molecular building block uptake by cells, the disulfide bond is cleaved by intracellular biothiols, which changes the structure and configuration of the molecular building block and allows the Xe atom to easily enter the cavity of the cryptophane cage. These changes result in stimulation of the ¹²⁹Xe NMR signal.

Due to the entrapped ¹²⁹Xe NMR signal cannot be observed by direct detection method, the Hyper-CEST method was used. Firstly, the GSH concentration-dependent Hyper-CEST spectra were obtained (Figures 2A and S4). Before Molego 1 reacted with GSH, a resonance peak appeared near 73 ppm, and the CEST effect was approximately 10%. In contrast, after Molego 1 incubated with GSH, the CEST effect rapidly increased with GSH concentration (Figure 2A), and increased slowly while the concentration of GSH reached 50 equiv (Figure 2B). Interestingly, upon incubation of Molego 1 with other biothiols, such as Cys and Hcy, the CEST effect at 72 ppm was also enhanced several-fold (Figure S5A), but did not exhibit any changes while Molego 1 treated with other nonthiol amino acids (Figure S5B).

A Hyper-CEST experiment was performed to test the sensitivity of Molego 1. We found that a 33% CEST effect was produced by 1 μ M Molego 1 with a cw-saturation pulse (13 μ T, 10 s) (Figure 2C). Time-dependent saturation transfer experiment was applied to investigate the detection threshold of Molego 1. After the stock solution of Molego 1 was reacted with GSH (100 equiv.), the time-dependent saturation transfer spectra for the diluted solution of Molego 1 (500 nM, 10 nM, 200 pM, and 100 pM) were obtained. For each sample, saturation profiles were collected by employing saturation pulses at the 129 Xe@cage frequency for incremental saturation times. The value 100 pM represents the detection threshold of Molego 1 (Figure S6), decreasing 1-fold compared to the value from previous studies (Zeng et al., 2017).

After treatment of Molego 1 with different concentrations of GSH, Hyper-CEST MRI scans were obtained. We found that the imaging signal increased with GSH concentration (Figure 2D), and the average change trend of CEST effect was similar to that of the CEST spectra shown in Figure 2B, but the absolute values were different because the image intensities were related to many factors, such as the imaging pulse sequences and MRI hardware settings.



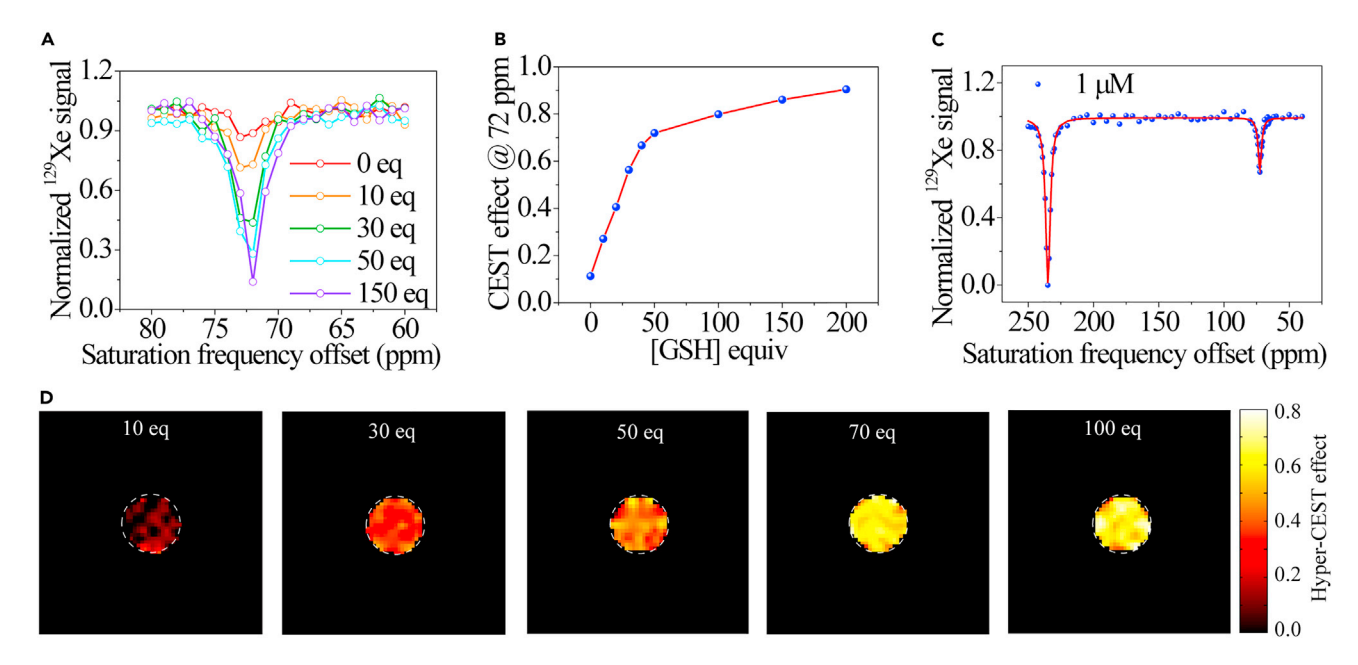


Figure 2. Hyper-CEST spectra and MRI for different concentrations of GSH

- (A) Hyper-CEST spectra of 1 (5 μ M) in response to different concentrations of GSH.
- (B) Hyper-CEST effect at 72 ppm after 1 reacted with different concentrations of GSH.
- (C) Hyper-CEST spectrum after 1 (1 μ M) reacted with GSH (0.1 mM).
- (D) Hyper-CEST MR phantom images for 1 (5 μ M) in response to different concentrations of GSH.

Optical spectroscopic studies

Optical spectroscopy of Molego 1 was performed to confirm the results obtained from \$129\$Xe NMR. We found that the absorption spectrum of Molego 1 was redshifted by 60 nm after reaction with GSH (Figure S9A), and the fluorescence intensity of it increased 67-fold (Figure S9B). Similar spectroscopic changes were observed upon the addition of other biothiols, such as Hcy and Cys. However, the optical spectra did not show any obvious change while Molego 1 exposed to nonthiol amino acids (Figure S10). Additionally, the fluorescence intensity of Molego 1 was related to the concentration of GSH (Figure S11A). After the concentration of GSH reached 2 mM (400 equiv.), the fluorescence intensity showed almost no obvious increase (Figure S11B). Following the addition of different concentrations of GSH, the fluorescence intensity of Molego 1 increased slowly with the passage of time (Figure S12A). After addition of Cys and Hcy to the solution of Molego 1, similar results were obtained (Figure S12B). Molego 1 was stable between pH 4.0 and 9.3 in the absence of GSH. But the fluorescence intensity at 550 nm increased greatly across the pH range of 6.0–9.3 when GSH was present (Figure S13). Most importantly, Molego 1 was stable in serum solution (Figure S14). These results suggest that Molego 1 can be used to detect biothiols without interference from nonthiol amino acids and pH.

LC-MS analysis

The product was analyzed via LC-MS after Molego 1 was reacted with GSH. Two peaks appeared at 6.05 min and 1.35 min in the HPLC chromatogram during the reaction of Molego 1 with GSH for 10 min (Figure \$15A). The peak at 6.05 min was assigned to Molego 1, and the peak at 1.35 min was assigned to compound 2, which was released from Molego 1. These results were confirmed by mass analysis (Figures \$15B and \$15C). A single peak appeared at 1.36 min, whereas the peak at 6.05 min disappeared after the reaction of Molego 1 with GSH was completed (Figure \$15D). Therefore, we can conclude that cleavage of the disulfide bond of Molego 1 by GSH was followed by intramolecular cyclization. Compound 2 was released from Molego 1 at the same time, making the fluorescence signal of the fluorescent moiety activated (Scheme \$2).

¹H-¹H NOESY experiments

The entrapped ¹²⁹Xe NMR signal of Molego 1 obtained by the direct detection method was too weak, which was unusual. We inferred that the configuration of Molego 1 in solution was not suitable for the capture of Xe atoms. The entry of Xe into the cryptophane cage was hindered before the probe reacted with



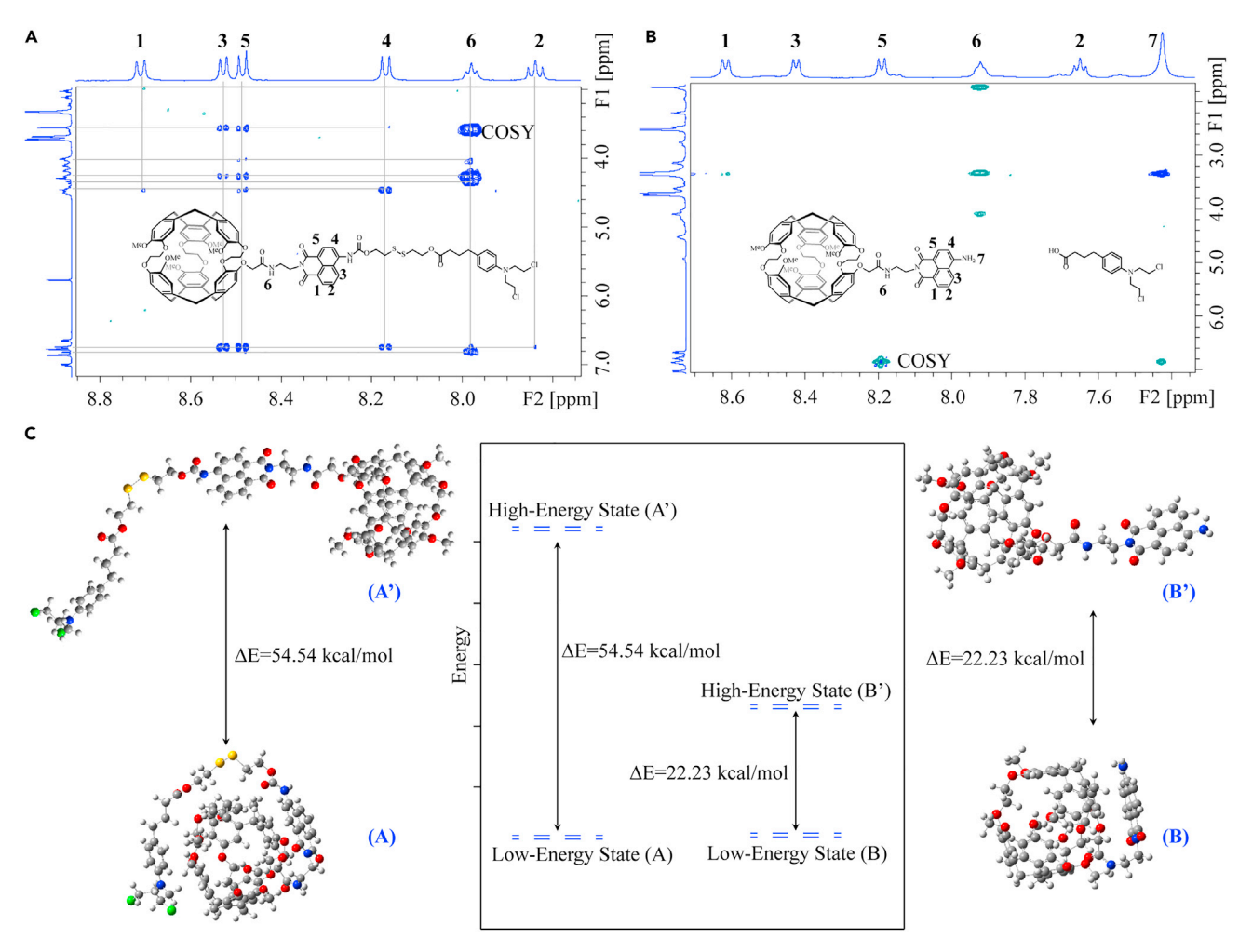


Figure 3. ¹H–¹H NOESY spectra and DFT calculation

- (A) ¹H–¹H NOESY of Molego **1** (4 mM) in DMSO-d6.
- (B) ¹H-¹H NOESY of compound 2 and CRB in DMSO-d6.
- (C) Configuration of Molego 1 before and after reaction with GSH calculated via DFT at the low-energy state.

biothiols, making it impossible to observe the signal of entrapped ¹²⁹Xe. When the structure and configuration of Molego 1 changed into compound 2 after it reacted with biothiols, as the Xe atom entered cryptophane cavities more easily, it was possible to observe a small signal.

¹H–¹H NOESY experiments were performed to confirm the inference. The aromatic protons of naphthalimide had a strong nuclear overhauser effect (NOE) with aromatic and aliphatic protons of the cryptophane cage before Molego 1 reacted with biothiols (Figures 3A and S17). After Molego 1 was reacted with biothiols, compound 2 and CRB derivant were released from Molego 1, so a mixture of compound 2 and CRB was used instead of the product solution of Molego 1. Most of the NOE signals had disappeared (Figures 3B and S19), which demonstrated that the configuration of 2 changed significantly compared to that of Molego 1. Encouraged by these results, we concluded that the linker of Molego 1 was long enough and flexible to fold on the cryptophane cage, which made it difficult for the Xe atom to enter the cryptophane cage. After Molego 1 reacted with biothiols, the disulfide bond of it cleaved, which made the linker shorter. The short linker could not fold on the cryptophane cage and block the entering of Xe. Therefore, the entrapped ¹²⁹Xe signal switched on after Molego 1 reacted with biothiols.

Theoretical calculation

The configurations of Molego 1 and compound 2 were theoretically optimized by the ω B97XD hybrid density function combined with the standard 6-31G(d,p) basis sets. Molego 1 was in a folded configuration, and



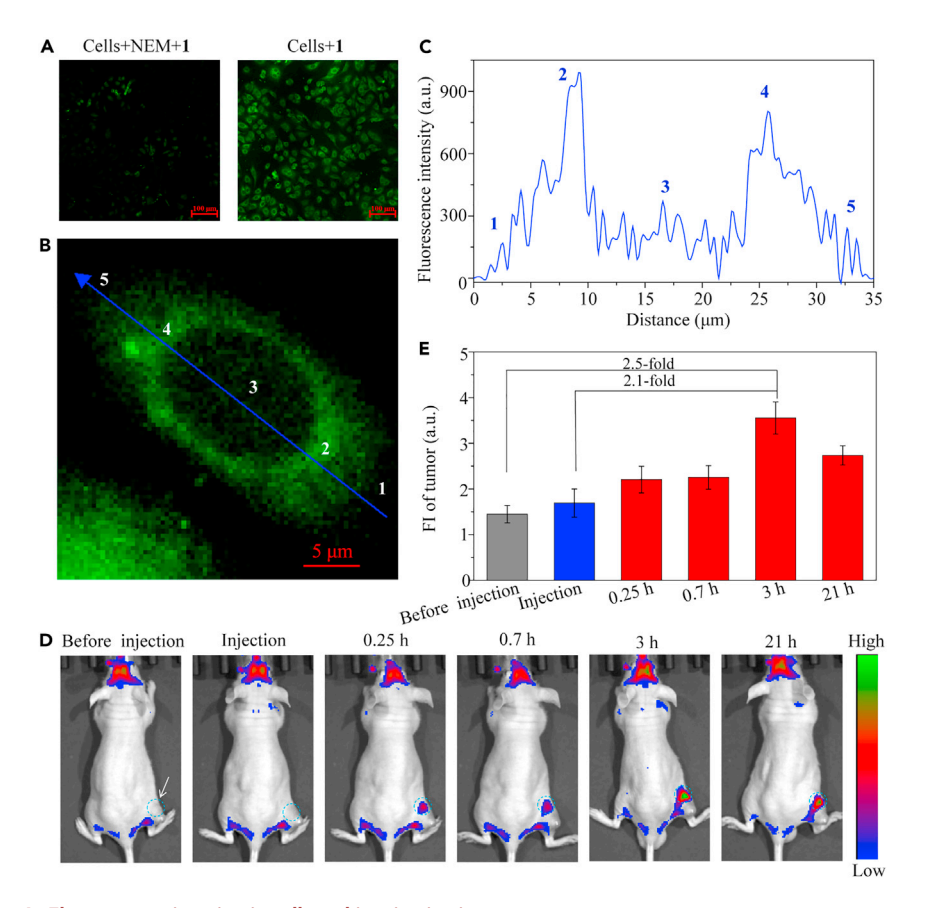


Figure 4. Fluorescence imaging in cells and in mice in vivo

(A) Fluorescence images of A549 cells treated with NEM and 1. Scale bars, 100 μ m. (B and C) Quantitative analysis of the fluorescence intensity of 1 in live cells. Scale bars, 5 μ m. (D) Time-dependent fluorescence images of 1 (100 μ M, 100 μ L) in A549 tumor-bearing model nude mice. (E) Time-dependent fluorescence intensity of the tumor after injection. The error bars are based on the standard deviations (SD) of 2 mice.

the linker was folded on the cryptophane cage in the low-energy state, which conferred on the naphthalimide moiety a strong NOE with the cryptophane cage. The difference in energy between the low-energy state and high-energy state was 54.54 kcal/mol (Figure 3C). Compound 2 was released from Molego 1 after 1 reacted with biothiols, and 2 was in the low-energy state in a folded configuration. Here, the short linker also underwent NOE with the cryptophane cage. However, the difference in energy between the high-energy state and low-energy state was 22.23 kcal/mol (Figure 3C). In this case, the compound 2 had a high chance of switching to the high-energy state. Therefore, the NOE of the short linker with the cryptophane cage was not strong enough to be observed in the NOESY experiment (Figures 3B and S19). The result of the theoretical calculation was consistent with the NOESY experiment and ¹²⁹Xe NMR experiment, which demonstrated that the ¹²⁹Xe NMR signal of entrapped Xe was suppressed by the interaction between the cryptophane and conjugated naphthalimide but not caused by aggregation.

Fluorescence imaging studies in cell and in vivo

To investigate the capability of Molego 1 for biothiol detection in live cells, the cellular fluorescence imaging was performed. After the cells were treated with Molego 1, strong fluorescence signals appeared in the cells (Figure 4A). While the cells were treated with N-ethylmaleimide (NEM, a popular thiol blocking agent) followed by Molego 1, the fluorescence signal of it in cells decreased significantly (Figure 4A). In addition, the fluorescence intensity of Molego 1 across the line in Figure 4B shows high green fluorescence intensity (Figure 4C). These results indicated that Molego 1 could be transfected into A549 cells effectively and responded well to biothiols in the cytoplasm.



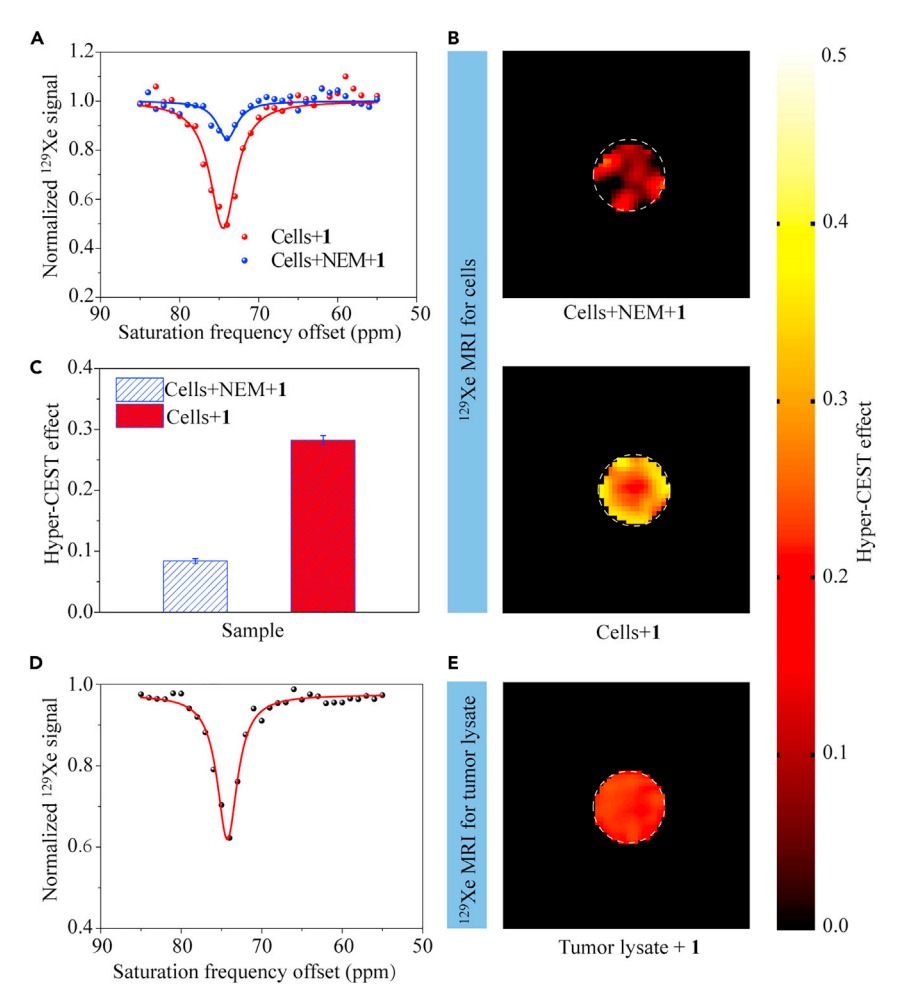


Figure 5. Hyper-CEST NMR and MRI for cells and tumor lysate

- (A) Hyper-CEST spectra of A549 cells treated with NEM and 1 (30 $\mu M).$
- (B) Hyper-CEST MR phantom images for 1 (30 μ M) in cells.
- (C) Average Hyper-CEST effect calculated from Hyper-CEST images. The error bars are based on the standard deviations (SD) of 2 samples.
- (D) Hyper-CEST spectra for A549 tumor lysate with ${\bf 1}.$
- (E) Hyper-CEST MR phantom images for A549 tumor lysate with 1.

Additionally, biothiol detection by Molego 1 *in vivo* was also performed in living mice bearing subcutaneous A549 tumors. After the mixed solution of Molego 1 (100 μ M) and GSH (10 mM) was injected into the tumor, fluorescence images were obtained immediately. The fluorescence intensity of the tumor increased with time (Figure 4D), and the maximum fluorescence, which appeared at 3 h post injection, was 2.5-fold stronger than that in the tumor without injection (Figure 4E). This demonstrated that Molego 1 could be stimulated by GSH *in vivo* and shows promise for application in biothiol imaging *in vivo*.

Hyperpolarized 129Xe NMR/MRI in cells and ex vivo

Cellular Hyper-CEST NMR and MRI were performed to investigate the capability of Molego 1 for biothiol detection in live cells too. After A549 cells were incubated with 1, only a single resonance appeared at approximately 74 ppm (Figure 5A), attributed to ¹²⁹Xe@cryptophane-A in cells, and MRI showed a strong CEST effect (Figures 5B and 5C). In cells treated with NEM (3 mM) followed by 1, the CEST effect decreased significantly (Figure 5A), and MRI also showed a weak CEST effect (Figures 5B and 5C).

Additionally, the Hyper-CEST strategy was applied to investigate the Molego 1 response to biothiols in tumors. After Molego 1 was injected into a tumor for 3 h, the tumor was resected and homogenized.





Then, 1 mL of water was added to the tumor homogenate, and the supernatant was obtained from the mixture by centrifugation. After that, Hyper-CEST experiments were performed while the supernatant was diluted 10 times. A significant NMR signal appeared at approximately 74 ppm (Figure 5D), which indicated that Molego 1 had reacted with the endogenous biothiols in the tumor and switched the ¹²⁹Xe NMR signal from off to on. Hyper-CEST MRI also showed an impressive signal intensity, with an almost 23% CEST effect (Figure 5E). All of these results unambiguously demonstrated that Molego 1 responded well to biothiols in live cells and *in vivo*.

Antitumor activity in cells and in vivo

Because Molego 1 was loaded with the FDA-approved chemotherapy agent, CRB, the antitumor activity was investigated. We found that the cells exhibited apoptosis after incubation with 1 (Figures S22 and S23). The antitumor activity of 1 was consistent with that of the anticancer agent CRB (Figure S24). Then, we carried out animal experiments to verify the antitumor activity of 1 *in vivo*. Molego 1 exhibited obvious tumor growth inhibition that was consistent with the effect of CRB (Figures S25–S29). More importantly, Molego 1 caused no obvious damage to the major organs, including the heart, liver, spleen, lung, and kidney (Figure S30), and the major blood counts, hematology markers of the liver and renal function showed no obvious change (Figure S31).

Conclusions

A molecular building block for biothiol NMR detection in live cells is presented herein. This molecular building block exhibited high stability over a broad pH range and showed high sensitivity for biothiols. When the molecular building block reacted with biothiols, the disulfide bond was cleaved, followed by intramolecular cyclization and loss of the disulfide linker. At the same time, the structure and configuration of the molecular building block changed, which resulted in the fluorescence and ¹²⁹Xe NMR signal switching from off to on. Impressively, this molecular building block showed high NMR detection sensitivity, and the detection threshold was 100 pM, indicating promise for *in vivo* application in the future. Most importantly, using this modular design, each functional module in the probe acts as a building block, linked into a whole through simple and effective chemical bonds. Different module can be chosen according to different goals, in order to build a suitable molecular building block for the problem at hand. This study provides a new flexible strategy for probe construction and expands the set of hyperpolarized ¹²⁹Xe molecular probes available for clinical imaging.

Limitations of the study

As we known, various diseases are directly correlated to the abnormal biothiol levels in cells. In this study, the Molego 1 can detect biothiols in cells selectively but cannot specifically identify different disease. In our future work, targeted modules will be selected for specific disease biomarkers detection, and disease-specific molecular building block will be constructed.

STAR*METHODS

Detailed methods are provided in the online version of this paper and include the following:

- KEY RESOURCES TABLE
- RESOURCE AVAILABILITY
 - Lead contact
 - O Materials availability
 - O Data and code availability
- EXPERIMENTAL MODEL AND SUBJECT DETAILS
 - O Cell lines
 - Animals
- METHOD DETAILS
 - Materials availability
 - O Synthesis and characterization of all compounds
 - O Hyper-CEST NMR and MRI studies in solution
 - O Optical spectra studies
 - LC-MS analysis
 - O Computational methods



- O Fluorescence imaging of GSH in cell
- O Fluorescence imaging of GSH in vivo
- O Cellular Hyper-CEST spectra and MRI studies
- O Tumor lysate Hyper-CEST spectra and MRI studies
- O Antitumor activity studies in vivo
- QUANTIFICATION AND STATISTICAL ANALYSIS

SUPPLEMENTAL INFORMATION

Supplemental information can be found online at https://doi.org/10.1016/j.isci.2021.103515.

ACKNOWLEDGMENTS

This work is supported by National Key R&D Program of China (2018YFA0704000), National Natural Science Foundation of China (91859206, 81625011, 81730048, 81825012, 21921004, 82001923, 81971705), Key Research Program of Frontier Sciences, CAS (ZDBS-LY-JSC004). X.Z. acknowledges the support from the Tencent Foundation through the XPLORER PRIZE. L.-S.B. acknowledges partial funding from the National Science Foundation (NSF) grant CHE-2002313. We acknowledge the help of Prof. Dr. Xianfeng Yi (Innovation Academy for Precision Measurement Science and Technology, CAS) for theoretical calculation.

AUTHOR CONTRIBUTIONS

X. Zhou conceived the idea and led the project. Q. Zeng, Q. Guo, Y. Yuan, B. Wang and M. Sui performed research. Q. Zeng, Q. Guo, X. Lou and X. Zhou analyzed data. Q. Zeng, Q. Guo, L.-S. Bouchard and X. Zhou prepared the manuscript and all authors contributed to the final version.

DECLARATION OF INTERESTS

The authors declare no competing interests.

Received: September 3, 2021 Revised: November 2, 2021 Accepted: November 22, 2021 Published: December 17, 2021

REFERENCES

Adiri, T., Marciano, D., and Cohen, Y. (2013). Potential ¹²⁹Xe-NMR biosensors based on secondary and tertiary complexes of a water-soluble pillar[5]arene derivative. Chem. Commun. 49, 7082–7084.

Chai, J.D., and Head-Gordon, M. (2008). Longrange corrected hybrid density functionals with damped atom-atom dispersion corrections. Phys. Chem. Chem. Phys. 10, 6615–6620.

Chambers, J.M., Hill, P.A., Aaron, J.A., Han, Z., Christianson, D.W., Kuzma, N.N., and Dmochowski, I.J. (2009). Cryptophane xenon-129 nuclear magnetic resonance biosensors targeting human carbonic anhydrase. J. Am. Chem. Soc. 131, 563–569.

Du, K., Zemerov, S.D., Carroll, P.J., and Dmochowski, I.J. (2020). Paramagnetic shifts and guest exchange kinetics in Co_nFe_{4-n} metalorganic capsules. Inorg. Chem. *59*, 12758–12767.

Gomes, M.D., Dao, P., Jeong, K., Slack, C.C., Vassiliou, C.C., Finbloom, J.A., Francis, M.B., Wemmer, D.E., and Pines, A. (2016). ¹²⁹Xe NMR relaxation-based macromolecular sensing. J. Am. Chem. Soc. *138*, 9747–9750.

Kotera, N., Dubost, E., Milanole, G., Doris, E., Gravel, E., Arhel, N., Brotin, T., Dutasta, J.P.,

Cochrane, J., Mari, E., et al. (2015). A doubly responsive probe for the detection of Cys4-tagged proteins. Chem. Commun. *51*, 11482–11094.

Kunth, M., Döpfert, J., Witte, C., Rossella, F., and Schröder, L. (2012). Optimized use of reversible binding for fast and selective NMR localization of caged xenon. Angew. Chem. Int. Ed. *51*, 8217–

Kunth, M., Witte, C., Hennig, A., and Schröder, L. (2015). Identification, classification, and signal amplification capabilities of high-turnover gas binding hosts in ultra-sensitive NMR. Chem. Sci. *6*, 6069–6075.

Lee, M.H., Yang, Z., Lim, C.W., Lee, Y.H., Dongbang, S., Kang, C., and Kim, J.S. (2013). Disulfide-cleavage-triggered chemosensors and their biological applications. Chem. Rev. 113, 5071–5109.

Li, H., Zhang, Z., Zhong, J., Ruan, W., Han, Y., Sun, X., Ye, C., and Zhou, X. (2016a). Oxygen-dependent hyperpolarized ¹²⁹Xe brain MR. NMR Biomed. *29*, 220–225.

Li, H., Zhang, Z., Zhao, X., Sun, X., Ye, C., and Zhou, X. (2016b). Quantitative evaluation of radiation-induced lung injury with hyperpolarized xenon magnetic resonance. Magn. Reson. Med. 76, 408–416.

Li, H., Zhang, Z., Zhao, X., Han, Y., Sun, X., Ye, C., and Zhou, X. (2018). Quantitative evaluation of pulmonary gas-exchange function using hyperpolarized ¹²⁹Xe CEST MRS and MRI. NMR Biomed. *31*, e3961.

Li, H., Zhao, X., Wang, Y., Lou, X., Chen, S., Deng, H., Shi, L., Xie, J., Tang, D., Zhao, J., et al. (2021). Damaged lung gas exchange function of discharged COVID-19 patients detected by hyperpolarized ¹²⁹Xe MRI. Sci. Adv. 7, eabc8180.

Meldrum, T., Seim, K.L., Bajaj, V.S., Palaniappan, K.K., Wu, W., Francis, M.B., Wemmer, D.E., and Pines, A. (2010). A xenon-based molecular sensor assembled on an MS2 viral capsid scaffold. J. Am. Chem. Soc. 132, 5936–5937.

Niu, L., Chen, Y., Zheng, H., Wu, L., Tung, C.H., and Yang, Q. (2015). Design strategies of fluorescent probes for selective detection among biothiols. Chem. Soc. Rev. 44, 6143–6160.

Palaniappan, K.K., Francis, M.B., Pines, A., and Wemmer, D.E. (2014). Molecular sensing using hyperpolarized xenon NMR spectroscopy. Isr. J. Chem. *54*, 104–112.



Qing, K., Ruppert, K., Jiang, Y., Mata, J.F., Miller, W., Shim, Y.M., Wang, C., Ruset, I.C., Hersman, F.W., Altes, T.A., et al. (2014). Regional mapping of gas uptake by blood and tissue in the human lung using hyperpolarized xenon-129 MRI. J. Magn. Reson. Imaging *39*, 346–359.

Riggle, B.A., Wang, Y., and Dmochowski, I.J. (2015). A "smart" ¹²⁹Xe NMR biosensor for pH-dependent cell labeling. J. Am. Chem. Soc. *137*, 5542–5548.

Roukala, J., Zhu, J., Giri, C., Rissanen, K., Lantto, P., and Telkki, V.-V. (2015). Encapsulation of xenon by a self-assembled Fe_aL_b metallosupramolecular cage. J. Am. Chem. Soc. 137, 2464–2467.

Roy, V., Brotin, T., Dutasta, J.P., Charles, M.H., Delair, T., Mallet, F., Huber, G., Desvaux, H., Boulard, Y., and Berthault, P. (2007). A cryptophane biosensor for the detection of specific nucleotide targets through xenon NMR spectroscopy. Chemphyschem *8*, 2082–2085.

Rose, H.M., Witte, C., Rossellaa, F., Klippel, S., Freund, C., and Schröder, L. (2014). Development of an antibody-based, modular biosensor for ¹²⁹Xe NMR molecular imaging of cells at nanomolar concentrations. Proc. Natl. Acad. Sci. U S A *111*, 11697–11702.

Schlundt, A., Kilian, W., Beyermann, M., Sticht, J., Gunther, S., Hopner, S., Falk, K., Roetzschke, O., Mitschang, L., and Freund, C. (2009). A xenon-129 biosensor for monitoring MHC-peptide interactions. Angew. Chem. Int. Ed. 48, 4142– 4145.

Schnurr, M., Sloniec-Myszk, J., Doepfert, J., Schröder, L., and Hennig, A. (2015). Supramolecular assays for mapping enzyme activity by displacement-triggered change in hyperpolarized ¹²⁹Xe magnetization transfer NMR spectroscopy. Angew. Chem. Int. Ed. *54*, 13444–13447.

Schröder, L., Lowery, T.J., Hilty, C., Wemmer, D.E., and Pines, A. (2006). Molecular imaging using a targeted magnetic resonance hyperpolarized biosensor. Science *314*, 446–449.

Schröder, L. (2013). Xenon for NMR biosensing—inert but alert. Phys. Med. 29, 3–16.

Seward, G.K., Bai, Y., Khan, N.S., and Dmochowski, I.J. (2011). Cell-compatible,

integrin-targeted cryptophane-¹²⁹Xe NMR biosensors. Chem. Sci. 2, 1103–1110.

Shapiro, M.G., Ramirez, R.M., Sperling, L.J., Sun, G., Sun, J., Pines, A., Schaffer, D.V., and Bajaj, V.S. (2014). Genetically encoded reporters for hyperpolarized xenon magnetic resonance imaging. Nat. Chem. 6, 629–634.

Spence, M.M., Rubin, S.M., Dimitrov, I.E., Ruiz, E.J., Wemmer, D.E., Pines, A., Yao, S., Tian, F., and Schultz, P.G. (2001). Functionalized xenon as a biosensor. Proc. Natl. Acad. Sci. U S A 98, 10654–10657.

Stevens, T.K., Ramirez, R.M., and Pines, A. (2013). Nanoemulsion contrast agents with sub-picomolar sensitivity for xenon NMR. J. Am. Chem. Soc. 135, 9576–9579.

Taratula, O., and Dmochowski, I.J. (2010). Functionalized ¹²⁹Xe contrast agents for magnetic resonance imaging. Curr. Opin. Chem. Biol. *14*, 97–104.

Wang, Y., Roose, B.W., Palovcak, E.J., Carnevale, V., and Dmochowski, I.J. (2016). A genetically encoded β -lactamase reporter for ultrasensitive ¹²⁹Xe NMR in mammalian cells. Angew. Chem. Int. Ed. *5*, 8984–8987.

Wei, Q., Seward, G.K., Hill, P.A., Patton, B., Dimitrov, I.E., Kuzma, N.N., and Dmochowski, I.J. (2006). Designing ¹²⁹Xe NMR biosensors for matrix metalloproteinase detection. J. Am. Chem. Soc. *128*, 13274–13283.

Witte, C., Martos, V., Rose, H.M., Reinke, S., Klippel, S., Schröder, L., and Hackenberger, C.P.R. (2015). Live-cell MRI with xenon Hyper-CEST biosensors targeted to metabolically labeled cell-surface glycans. Angew. Chem. Int. Ed. 54, 2806–2810.

Xiao, S., Deng, H., Duan, C., Xie, J., Zhang, H., Sun, X., Ye, C., and Zhou, X. (2018). Considering low-rank, sparse and gas-inflow effects constraints for accelerated pulmonary dynamic hyperpolarized ¹²⁹Xe MRI. J. Magn. Reson. *290*, 20

Xie, J., Li, H., Zhang, H., Zhao, X., Shi, L., Zhang, M., Xiao, S., Deng, H., Wang, K., Yang, H., et al. (2019). Single breath-hold measurement of pulmonary gas exchange and diffusion in humans with hyperpolarized ¹²⁸Xe MR. NMR Biomed. *32*, e4068.

Yang, Y., Zhang, Y., Wang, B., Guo, Q., Yuan, Y., Jiang, W., Shi, L., Yang, M., Chen, S., Lou, X., et al. (2021). Coloring ultrasensitive MRI with tunable metal-organic frameworks. Chem. Sci. 12, 4300–4308.

Yang, S., Jiang, W., Ren, L., Yuan, Y., Zhang, B., Luo, Q., Guo, Q., Bouchard, L.-S., Liu, M., and Zhou, X. (2016). Biothiol xenon MRI sensor based on thiol-addition reaction. Anal. Chem. 88, 5835– 5840.

Yang, S., Yuan, Y., Jiang, W., Ren, L., Deng, H., Bouchard, L.-S., Zhou, X., and Liu, M. (2017). Hyperpolarized 129 Xe magnetic resonance imaging sensor for H_2 S. Chem. Eur. J. 23, 7648–7652.

Zeng, Q., Guo, Q., Yuan, Y., Yang, Y., Zhang, B., Ren, L., Zhang, X., Luo, Q., Liu, M., Bouchard, L.-S., et al. (2017). Mitochondria targeted and intracellular biothiol triggered hyperpolarized ¹²⁹Xe magnetofluorescent biosensor. Anal. Chem. *89*, 2288–2295.

Zeng, Q., Bie, B., Guo, Q., Yuan, Y., Han, Q., Han, X., Chen, M., Zhang, X., Yang, Y., Liu, M., et al. (2020a). Hyperpolarized Xe NMR signal advancement by metal-organic framework entrapment in aqueous solution. Proc. Natl. Acad. Sci. U S A 117, 17558–17563.

Zeng, Q., Guo, Q., Yuan, Y., Zhang, X., Jiang, W., Xiao, S., Zhang, B., Lou, X., Ye, C., Liu, M., et al. (2020b). A small molecular multifunctional tool for pH detection, fluorescence imaging, and photodynamic therapy. ACS Appl. Biol. Mater. 3, 1779–1786.

Zhang, S., Ong, C.N., and Shen, H.M. (2004). Critical roles of intracellular thiols and calcium in parthenolide-induced apoptosis in human colorectal cancer cells. Cancer Lett. 208, 143–153.

Zhang, B., Guo, Q., Luo, Q., Zhang, X., Zeng, Q., Zhao, L., Yuan, Y., Jiang, W., Yang, Y., Liu, M., et al. (2018). An intracellular diamine oxidase triggered hyperpolarized ¹²⁹Xe magnetic resonance biosensor. Chem. Commun. *54*, 13654–13657.

Zhang, H., Yu, Q., Li, Y., Yang, Z., Zhou, X., Chen, S., and Jiang, Z. (2020). Fluorinated cryptophane-A and porphyrin-based theranostics for multimodal imaging-guided photodynamic therapy. Chem. Commun. *56*, 3617–3620.





STAR*METHODS

KEY RESOURCES TABLE

REAGENT or RESOURCE	SOURCE	IDENTIFIER
Chemicals, peptides, and recombinant proteins		
4-Dimethylaminopyridine	Sinopharm	Cat#30198425
Ethyl 2-bromoacetate	Sinopharm	Cat#80060616
Cryptophanol-A	Wuhan Liperen	N/A
1-(3-Dimethylaminopropyl)-3-	Shanghai Medpep	N/A
ethylcarbodiimide hydrochloride (EDCI)		
1-Hydroxybenzotriazole (HOBt)	GL Biochem	N/A
4-Bromonaphthalic anhydride	Aladdin Chemistry	Cat#B151969
N-ethylmaleimide	Aladdin Chemistry	Cat#E100552
Cremophor®EL	Aladdin Chemistry	Cat#C107105
N-Boc-ethylenediamine	Aladdin Chemistry	Cat#B113755
2-Hydroxyethyl disulfide	Aladdin Chemistry	Cat#B152479
Triphosgene	Aladdin Chemistry	Cat#T103041
N,N-Diisopropylethylamine (DIPEA)	Aladdin Chemistry	Cat#D109321
NaHS	J&K Scientific	Cat#A01553951
Chlorambucil	J&K Scientific	Cat#A01321407
Dimethyl sulfoxide (DMSO), spectral grade	Tianjin Kemiou	N/A
Experimental models: Cell lines		
A549	Shanghai Cell Bank	N/A
Experimental models: Organisms/strains		
BALB/c	Beijing Vital River	N/A
Software and algorithms		
OriginPro 2016	OriginLab	https://www.originlab.com
Matlab R2014a	MathWorks	https://ww2.mathworks.cn/en
Other		
AV-III400 (400 MHZ) spectrometer	Bruker	https://bruker.com
AV-III500 (500 MHz) spectrometer	Bruker	https://bruker.com
Evolution 220 UV-Vis spectrometer	ThermoFisherScientific	https://thermofisher.com
FS5 fluorescence spectrophotometer	Edinburgh Instruments	https://www.edinst.com
6530 Accurate-Mass Q-TOF spectrometer	Agilent	http://www.agilent.com

RESOURCE AVAILABILITY

Lead contact

Further information and requests for resources and reagents should be directed to and fulfilled by the lead contact, Prof. Dr Xin Zhou (xinzhou@wipm.ac.cn).

Materials availability

- This study did not generate new unique reagents. All reagents used in this study were commercially available and used without further purification.
- All other data supporting the findings of this study are available within the article and the supplemental information or from the lead contact upon reasonable request.





Data and code availability

- All data and experimental methods are available in the main text or in supplemental information. All data reported in this paper will be shared by the lead contact upon request.
- This paper does not report original code.
- Any additional information required to reanalyze the data reported in this work paper is available from the Lead Contact upon request.

EXPERIMENTAL MODEL AND SUBJECT DETAILS

Cell lines

All cell lines used in this study were purchased from Shanghai Cell Bank and cultured according to the provided protocols. The complete culture medium of A549 cell line was formulated as 10% fetal bovine serum (FBS) and 1% penicillin–streptomycin, an additional 2 mM L-glutamine, and 1 mM sodium pyruvate in F12K.

Animals

All mice used in this research were purchased from the Beijing Vital River Laboratory Animal Technology Co., Ltd. and fed on SPF grad mice feed (purchased from Wuhan WanQian JiaXing Bio-Technology Co., Ltd.). All BALB/c mice used in this study were male and aged 5 weeks before the experiments. All animal studies were conducted according to the experimental practices and standards approved by the Animal Welfare and Research Ethics Committee at Innovation Academy for Precision Measurement Science and Technology, Chinese Academy of Sciences.

METHOD DETAILS

Materials availability

4-Dimethylaminopyridine (DMAP), Ethyl 2-bromoacetate, were purchased from Sinopharm Chemical Reagent Co. Ltd.; Cryptophanol-A was purchased from Wuhan Liperen Sci-Tech Co. Ltd.; 1-(3-Dimethylaminopropyl)-3-ethylcarbodiimide hydrochloride (EDCI) was purchased from Shanghai Medpep Co. Ltd.; 1-Hydroxybenzotriazole (HOBt) was purchased from GL Biochem Ltd.; 4-Bromonaphthalic anhydride, Nethylmaleimide, Cremophor®EL, N-Boc-ethylenediamine, 2-Hydroxyethyl disulfide, Triphosgene, N,N-Diisopropylethylamine (DIPEA) were purchased from Aladdin Chemistry Co. Ltd.; NaHS, Chlorambucil were purchased from J&K Scientific Ltd. All reagents were of analytical grade. Dimethyl sulfoxide (DMSO) was purchased from Tianjin Kemiou Chemical Reagent Co. Ltd., this reagent was of spectral grade.

Synthesis and characterization of all compounds

Synthesis and characterization of compound 3. After the 4-Bromonaphthalic anhydride (3.0 g, 10.8 mmol) was dispersed in 20 ml ethanol, the N-Boc-ethylenediamine (1.9 g, 11.9 mmol) was added to the mixture, and kept reflux for 10 h. While the reaction completed, a precipitate was formed. The result mixture was cooled to room temperature, filtered and the filter cake was washed by ethanol for 3 times to give compound 3 as a gray solid (3.4 g, 75.6%). ¹H NMR (500 MHz, CDCl₃) δ 8.66 (dd, J = 7.3, 1.0 Hz, 1H), 8.57 (dd, J = 8.5, 1.0 Hz, 1H), 8.42 (d, J = 7.9 Hz, 1H), 8.04 (d, J = 7.9 Hz, 1H), 7.85 (dd, J = 8.4, 7.3 Hz, 1H), 4.35 (t, J = 5.7 Hz, 2H), 3.53 (m, 2H), 1.28 (s, 9H). ¹³C NMR (126 MHz, CDCl₃) δ 164.00, 156.05, 133.42, 132.25, 131.43, 131.13, 130.64, 130.42, 129.11, 128.10, 122.95, 122.09, 40.03, 39.57, 28.21. HRMS (ESI): [M+Na]⁺, cacld for C₁₉H₁₉N₂O₄BrNa, m/z 441.0426, found 441.0420.

Synthesis and characterization of compound 4. Compound 3 (3.0 g, 7.16 mmol) was dissolved in DMF (10 ml), and then NaN_3 (0.7 g, 10.73 mmol) was added. After the reaction completed at 60°C, 40 ml water was added to the solution, large amount of precipitate was formed, filtered and the filter cake was washed by ethanol for 3 times to give compound 4 as a yellowish solid. The product without further purification was taken to the next step directly.

Synthesis and characterization of compound 5. Compound 4 was dissolved in DMF (5 ml), and then NaHS (2 g, 35.8 mmol) was added carefully. The mixture was stirred at room temperature, and the reaction progress was monitored by TLC, after the reaction completed, large amount of water was added into the solution, yellow solid was precipitation, filtered and the filter cake was washed by ethanol for 3 times, and the solid was dried in vacuum dryer for 5 h to afford yellow solid as compound 5 (2 g, two step yield 52.6%).



 ^{1}H NMR (500 MHz, DMSO-d6) δ 8.60 (d, J = 8.3 Hz, 1H), 8.41 (d, J = 7.0 Hz, 1H), 8.18 (d, J = 8.3 Hz, 1H), 7.65 (dd, J = 7.6, 7.5 Hz, 1H), 7.39 (s, NH2, 2H), 6.89-6.78 (m, Ar+CONH, 2H), 4.09 (t, J = 6.0 Hz, 2H), 3.22 (m, 2H), 1.22 (s, 9H). ^{13}C NMR (126 MHz, DMSO-d6) δ 164.47, 163.58, 156.13, 152.98, 134.27, 131.30, 130.30, 129.56, 124.36, 122.54, 119.83, 108.51, 108.36, 77.86, 38.51, 28.60. HRMS (ESI): [M+Na]+, cacld for $C_{19}H_{21}N_{3}O_{4}N_{a}$, m/z 378.1430, found 378.1424.

Synthesis and characterization of compound 6. Compound 5 (355 mg, 1 mmol) and triphosgene (890 mg, 3 mmol) were dispersed in dry DCM (15 ml), and then DIPEA (905 mg, 7 mmol) was added dropwise in the solution under N_2 atmosphere. After the solution stirred at room temperature for 3 h, the unreacted phosgene gas (Caution: Toxic) was removed by bubbing N_2 through in the solution and neutralization in an NaOH bath. After that, a solution of 2-hydroxyethyl disulfide (771 mg, 5 mmol) in DCM/THF (v/v 1/1) was added to the mixture. After the solution stirred at room temperature for another 10 h, the solvent was evaporated under vacuum. The crude product was purified by silica gel column chromatography using DCM/MeOH (v/v 40/1) as eluent to give compound 6 as a yellowish solid (100 mg, 18.7%). ¹H NMR (500 MHz, CDCl₃) δ 8.65 (d, J = 7.2 Hz, 1H), 8.62 (d, J = 8.3 Hz, 1H), 8.38 (d, J = 8.2 Hz, 1H), 8.24 (d, J = 8.5 Hz, 1H), 7.78 (t, J=7.9 Hz, 1H), 7.71 (s, NH, 1H), 4.96 (s, OH, 1H), 4.57 (t, J = 6.3 Hz, 2H), 4.36 (t, J = 5.7 Hz, 2H), 3.96 (t, J = 5.7 Hz, 2H), 3.53 (m, 2H), 3.08 (t, J = 6.3 Hz, 2H), 2.96 (t, J = 5.7 Hz, 2H), 1.30 (s, 9H). ¹³C NMR (126 MHz, CDCl₃) δ 164.50, 164.02, 156.07, 152.97, 139.05, 132.74, 131.53, 129.05, 126.69, 126.27, 123.23, 123.03, 117.77, 116.92, 63.88, 60.60, 41.57, 39.83, 37.52, 28.24. HRMS (ESI): [M+Na]⁺, cacld for $C_{24}H_{29}N_{3}O_{7}S_{2}N_{8}$, m/z 558.1345, found 558.1341.

Synthesis and characterization of compound 7. Chlorambucil (56.9 mg, 0.187 mmol) was dissolved in 5 mL dry DCM, and then EDCI (107.5 mg, 0.561 mmol) was added. The mixture was stirred at 0 $^{\circ}$ C under N_2 atmosphere for 30 min, and then HOBt (75.8 mg, 0.561 mmol) was added, the mixture was stirred at 0° C under N_2 atmosphere for another hour. After that, compound 6 (100 mg, 0.187 mmol) and DMAP (68.4 mg, 0.561 mmol) were added. The mixture was stirred at RT for another 10 h. After the reaction completed, 50 mL ethyl acetate was added, the organic layer was washed with water for 3 times and dried with anhydrous Na₂SO₄. The solvent was evaporated under vacuum. The residue was purified with silica gel column chromatography using ethyl acetate /hexane (v/v 1/1) to give compound 7 as a yellowish solid (120 mg, 78.2%). ¹H NMR $(500 \text{ MHz}, \text{CDCl}_3)$ δ 8.61 (d, J = 5.1 Hz, 1H), 8.60 (d, J = 6.5 Hz, 1H), 8.37 (d, J = 6.5 Hz, 1H)8.3 Hz, 1H), 8.34 (d, J = 8.5 Hz, 1H), 7.94 (s, 1H), 7.74-7.69 (m, 1H), 7.02 (d, J = 8.6 Hz, 2H), 6.65 (d, J = 8.5 Hz, 1H), 7.94 (s, 1H), 7.74-7.69 (m, 1H), 7.02 (d, J = 8.6 Hz, 2H), 6.65 (d, J = 8.5 Hz, 1H), 7.94 (s, 1H), 7.74-7.69 (m, 1H), 7.02 (d, J = 8.6 Hz, 2H), 6.65 (d, J = 8.5 Hz, 1H), 7.94 (s, 1H), 7.74-7.69 (m, 1H), 7.02 (d, J = 8.6 Hz, 2H), 6.65 (d, J = 8.5 Hz, 1H), 7.94 (s, 1H), 7.74-7.69 (m, 1H), 7.02 (d, J = 8.6 Hz, 2H), 6.65 (d, J = 8.6 8.6 Hz, 2H), 4.55 (t, J = 6.1 Hz, 2H), 4.42 (t, J = 6.9 Hz, 2H), 4.38-4.33 (m, 2H), 3.69 (t, J = 6.7 Hz, 4H), 3.62 (t, J = 6.7 Hz, 4H), 3.53 (s, 2H), 3.05 (t, J = 6.1 Hz, 2H), 2.97 (t, J = 6.9 Hz, 2H), 2.53 (t, J = 7.6 Hz, 2H), 2.35 (t, J = 7.5 Hz, 2H), 1.94-1.84 (m, 2H), 1.30 (s, 9H). ¹³C NMR (126 MHz, CDCl₃) δ 173.80, 164.52, 164.05, 156.07, 152.98, 143.95, 139.27, 132.73, 131.50, 130.98, 129.72, 129.07, 126.60, 126.55, 123.16, 123.09, 117.73, 116.96, 112.69, 79.12, 62.95, 62.54, 53.84, 40.29, 39.78, 37.66, 36.50, 33.94, 33.61, 29.71, 28.25. HRMS (ESI): HRMS (ESI): $[M+Na]^+$, cacld for $C_{38}H_{46}N_4O_8S_2Cl_2Na$, m/z 843.2032, found 843.2052.

Synthesis and characterization of compound 8. Compound 7 (60 mg, 0.073 mmol) was dispersed in 3 M HCl ethyl acetate solution (10 ml), the mixture was stirred at room temperature for 30 min. After the reaction completed, filtered and the filter cake was washed by diethyl ether to afford yellowish solid as compound 8 (50 mg, 90.9%). The product was taken to the next step without further purification.

Synthesis and characterization of compound 9. Cryptophane-A (100 mg, 0.113 mmol) and ethyl 2-bromoacetate (38.4 mg, 0.23 mmol) were dissolved in 15 mL of acetone, and then K_2CO_3 (77.4 mg, 0.56 mmol) was added. After the mixture was reflux for 6 h, the mixture was cooled to room temperature, and 20 mL of ethyl acetate was added. The organic phase was washed with water (30 mL \times 3) and dried with anhydrous Na_2SO_4 , and the solvent was evaporated under vacuum to afford white solid. The solid was dispersed in 20 mL of 3 M NaOH aqueous THF (1/1), and then the solution was cooled to room temperature after refluxed for 10 h. Subsequently, HCl (0.1 M) was added dropwise until the solution became neutral, DCM (30 mL) was then added, and the organic layer was washed with water, and dried with anhydrous Na_2SO_4 , and the solvent was evaporated under vacuum to afford white solid as the compound 9 (88 mg, 83%). The product was taken on to the next step without further purification. The characterization data was identical to that reported in the literature (Zeng et al., 2017).

Synthesis and characterization of Molego 1. After the compound 9 (50 mg, 0.053 mmol) and EDCI (30.5 mg, 0.159 mmol) were dissolved in dry DCM (5 ml), the mixture was stirred at 0°C for 30 min, and





then HOBt (21.5 mg, 0.159 mmol) was added to the mixture and stirred for another 1 h. After that, compound 8 (44 mg, 0.058 mmol) and DIPEA (20.6 mg, 0.159 mmol) were added to the solution and stirred for another 10 h at room temperature. Finally, the solvent was evaporated under vacuum, and the crude product was purified by silica gel column chromatography using DCM/MeOH (v/v 50/1) as eluent to give Molego 1 as a yellowish solid (52 mg, 59.8%). ¹H NMR (500 MHz, CDCl₃) δ 8.64 (d, J = 7.2 Hz, 1H), 8.60 (d, J = 8.2 Hz, 1H), 8.37 (d, J = 8.9 Hz, 2H), 7.95 (s, 1H), 7.74 (t, J = 7.9 Hz, 1H), 7.42 (t, J = 5.4 Hz, 1H),7.07 (d, J = 8.3 Hz, 2H), 6.88-6.66 (m, 12H), 6.62 (d, J = 6 Hz, 2H), 4.65-4.47 (m, 8H), 4.47-4.33 (m, 6H), 4.23-3.99 (m, 12H), 3.86-3.55 (m, 25H), 3.44-3.36 (m, 4H), 3.32 (m, 2H), 3.04 (t, J=6.0 Hz, 2H), 2.96 (t, J=6.0 Hz), 2.96 (6.8 Hz, 2H), 2.56 (t, J = 7.5 Hz, 2H), 2.35 (t, J = 7.4 Hz, 2H), 1.89 (m, 2H). 13 C NMR (126 MHz, CDCl₃) δ 173.79, 169.13, 164.48, 163.99, 152.99, 149.91, 149.71, 149. 63, 149.61, 149.49, 147.91, 147.43, 146.88, 146.78, 146.64, 146.57, 146.49, 143.61, 139.41, 134.58, 134.25, 134.23, 134.05, 133.87, 133.71, 132.77, 131.79, 131.78, 131.61, 131.58, 131.41, 131.25, 129.76, 129.08, 126.80, 126.66, 123.24, 123.04, 121.29, 121.14, 121.03, 120.67, 120.61, 120.50, 117.94, 117.61, 117.16, 114.78, 113.75, 113.68, 113.63, 113.05, 113.05, 69.84, 69.46, 69.43, 69. 27, 69.22, 69.19, 62.95, 62.54, 56.00, 55.69, 54.01, 53.44, 40.13, 39.46, 38.37, 37.65, 36.45, 36.26, 36.23, 36.18, 36.09, 35.94, 33.96, 33.60, 31.60, 29.71. HRMS (ESI): [M+H+2]⁺, cacld for $C_{88}H_{91}N_4O_{19}S_2Cl_2$, m/z 1643.5096, found 1643.5090, $[M+Na+2]^+$, cacld for $C_{88}H_{90}N_4O_{19}S_2Cl_2Na$, m/z 1665.4915, found 1665.4934.

Synthesis and characterization of compound 10. Compound 4 (100 mg, 0.28 mmol) was dispersed in 3 M HCl ethyl acetate solution (20 ml), the mixture was stirred at room temperature for 30 min. After the reaction completed, filtered and the filter cake was washed by diethyl ether to afford yellow solid as compound 10 (85 mg, 92.5%). The product was taken to the next step without further purification.

Synthesis and characterization of compound 2. Compound 9 (25 mg, 0.027 mmol) was dissolved in dry DCM (5 ml), and then EDCI (15.3 mg, 0.08 mmol) was added to the solution, the mixture was stirred at 0°C for 30 min, and then HOBt (10.8 mg, 0.08 mmol) was added to the mixture and stirred for another 1 h. After that, compound 10 (9.7 mg, 0.03 mmol) and DIPEA (20.6 mg, 0.159 mmol) were added to the solution. After the solution stirred at room temperature for another 10 h, the solvent was evaporated under vacuum. The crude product was purified by silica gel column chromatography using DCM/MeOH (v/v 30/1) as eluent to give compound 2 as a yellow solid (11 mg, 34.6%). 1 H NMR (500 MHz, CDCl₃) 3 8.65 (d, J = 7.1 Hz, 1H), 8.47 (d, J = 8.1 Hz, 1H), 8.13 (d, J = 8.2 Hz, 1H), 7.70-7.64 (t, J=7.1 Hz, 1H), 7.47 (t, J = 5.3 Hz, NH2, 2H), 6.90 (d, J = 8.1 Hz, 1H), 6.76-6.63 (m, 12H), 4.62-4.54 (m, 5H), 4.52-4.39 (m, 3H), 4.38-4.36 (m, 2H), 4.25-4.04 (m, 12H), 3.88-3.72 (m, 15H), 3.72-3.63 (m, 3H), 3.44-3.30 (m, 6H). HRMS (ESI): [M+Na]⁺, cacld for $C_{69}H_{65}N_3O_{15}N_a$, m/z 1198.4313, found 1198.4294.

Hyper-CEST NMR and MRI studies in solution

After the Molego 1 incubation with GSH at 37°C for 3 h in PBS buffer (pH=7.4, 20 mM, including 50% DMSO), the samples were transfer to 10 mm NMR tube, and the ¹²⁹Xe NMR/MRI were obtained. All ¹²⁹Xe NMR/MRI experiments were taken on a 9.4 T Bruker AV400 wide bore NMR spectrometer (Bruker Biospin, Ettlingen, Germany). For all experiments, the sample temperature was controlled by a VT unit installed on the NMR spectrometer and held fixed at 298 K. A gas mixture of 10% N₂, 88% He, and 2% Xe (26.4% ¹²⁹Xe natural abundance) (Spectra Gases) was used. Hyperpolarized ¹²⁹Xe gas was generated using a home-built ¹²⁹Xe hyperpolarizer (hyperpolarized ¹²⁹Xe nuclear spin polarization was 100,000 times greater than its thermal equilibrium polarization).

For the 129 Xe NMR experiment, the hyperpolarized gas was directly bubbled into a 10 mm NMR tube for 20 s followed by a 3 s delay to allow bubbles to collapse. And then, a zg sequence (rectangular pulse, the pulse length p1 = 31.8 μ s) was applied and the spectra were acquired, each spectrum was acquired using 16 scans. All NMR spectra were processed using 5 Hz Lorentz broadening.

For the Hyper-CEST NMR experiment, after the hyperpolarized 129 Xe gas was directly bubbled into a 10 mm NMR tube for 20 s, a delay of 3 s to allow the bubbles to collapse. A continuous-wave (cw) saturation pulse (6.5 μ T, 10 s) was swept across the chemical shift range of 60-80 ppm in 1-ppm steps, and then the spectrum was acquired in a single scan. All NMR spectra were processed using 5 Hz Lorentz broadening.

For the sensitivity test experiment, after the hyperpolarized 129 Xe was directly bubbled into a 10 mm NMR tube for 20 s, a delay of 3 s to allow the bubbles to collapse. And then, a continuous-wave (cw) saturation



pulse (13 μ T, 10 s) was swept across the chemical shift range of 40-250 ppm in 1, 2 or 5 ppm steps, and then the spectrum was acquired in a single scan. All NMR spectra were processed using 5 Hz Lorentz broadening.

For the detect limitation test experiment, after the hyperpolarized ^{129}Xe was directly bubbled into a 10 mm NMR tube for 20 s, a delay of 3 s to allow the bubbles to collapse. And then, a continuous-wave (cw) saturation pulse was applied, and then the spectrum was acquired in a single scan. Saturation frequencies of cw pulses were positioned +164 ppm and -164 ppm referenced to dissolved Xe peak, for off- and on-resonance (cw-saturation for 0-20 s in 1 s steps with a 13 μT field). All NMR spectra were processed using 5 Hz Lorentz broadening.

For the Hyper-CEST MRI experiment, 8 off-resonant (164 ppm) and 8 on-resonant (-164 ppm) (The chemical shift of dissolved 129 Xe was set as 0 ppm) scans were acquired and averaged. The image was acquired using a RARE sequence (slice thickness=25 mm, matrix size=32×32, in-plane resolution=0.9375×0.9375 mm², FOV=30×30 mm², centric k-space encoding, bandwidth=5400 Hz, echo time=4.65 ms, repetition time=28040 ms, centric k-space encoding, no partial Fourier transform acceleration, rare factor=8). For each excitation, after the hyperpolarized 129 Xe gas mixture was bubbled into solution for 20 s, a delay time (3 s) to allow bubbles to collapse. And then, a saturation pulse (13 μ T, 5 s) was used. Finally, the image was acquired. The MR images were processed on MATLAB (R2014a, MathWorks, Natick, MA). The image matrix 32×32 was interpolated into 64×64 image matrix. Hyper-CEST effect for on-resonant saturation was analyzed compared to off-resonant saturation for each pixel by the formula (CEST effect = (Intensity_off-Intensity_on)/Intensity_off) point by point. The mask was used in the post-processing which covers the image areas that do not belong to the sample phantom and the normalized signal intensities less than 0.2.

Optical spectra studies

All biologically relevant analytes [Val, Leu, Ile, Phe, Trp, Met, Pro, Gly, Ser, Thr, Tyr, Asn, Gln, His, Lys, Arg, Asp, Glu, Ala, Cys, Hcy, GSH,] stock solution were prepared in ultrapure water. Stock solution of Molego 1 was prepared in spectral grade DMSO. Absorption spectra were obtained on a Thermo Scientific evolution 220 UV-Vis spectrometer, and fluorescence spectra were recorded on an Edinburgh FS5 fluorescence spectrophotometer. The samples of absorption and fluorescence were stored in quartz cuvettes (3 mL volume). The excitation wavelength was 440 nm, and the excitation and emission slit widths were kept at 4 nm. After the Molego 1 incubated with different analytes in PBS buffer (pH=7.4, 20 mM, containing 50% DMSO) for 3 h at 37°C, the optical spectra were obtained at room temperature.

LC-MS analysis

HPLC experiments were taken on an Agilent HPLC (Agilent 1260 series) with an Agilent SB-C18 (1.8 μ m, 2.1 × 50 mm) column for analytical. The flow rate of HPLC was 0.1 mL/min. For the mobile phase, ultrapure water and MeOH were used to provide the solvent gradient (water/MeOH, 10/90). ESI mass spectrometric analyses were carried out using an Agilent 6530 Accurate-Mass Q-TOF spectrometer.

Computational methods

The configurations of Molego 1 and compound 2 were theoretically optimized by $\omega B97XD$ hybrid density function, combined with the standard 6-31G(d,p) basis sets. This method was a recently developed long-range-corrected hybrid functional by Chai and Head-Gordon (Chai and Head-Gordon, 2008), which implicitly accounts for empirical dispersion and can well describe long-range dispersion interactions with respect to the traditional density functional theory (DFT) methods.

Fluorescence imaging of GSH in cell

The human non-small lung cancer cells A549 were seeded on glass coverslips placed in the 6-well plates. After grown at 37°C in an atmosphere of 5% $\rm CO_2$ for 24 h, the regular culture mediums were removed. F12K medium containing the Molego 1 was added (Molego 1 was dissolved in DMSO, and then stock in F12K medium, including 1% DMSO, 1% Cremophor ® EL). For the control experiments, the cells were treated with N-ethylmaleimide (NEM) firstly, and then incubated with Molego 1. After 1 h of incubation at 37°C, the medium was removed, and the cells were fixed by paraformaldehyde for 10 min, and then the cells were washed by PBS at least three times. The cells fluorescence images were taken on a Nikon Confocal Laser Scanning Microscope (CLSM, Nikon, Japan).





Fluorescence imaging of GSH in vivo

The fluorescence imaging in vivo was investigated using a flank A549 BALB/c male nude mice tumor model. After the mixture solution of Molego 1 and GSH (Molego 1, 100 μ M, and GSH 10 mM, in 100 μ L of PBS solution, including 1% DMSO, 1% Cremophor®EL) was injected into the tumor directly, the fluorescence images were acquired by an IVIS Spectrum in epi-fluorescence mode, and the filters for excitation and emission are 430 and 540 nm, respectively.

Cellular Hyper-CEST spectra and MRI studies

The A549 cells were incubated in F12K supplemented with 10% fetal bovine serum and 1% penicillin-streptomycin at 37° C in an atmosphere of 5% CO₂ for 48 h. And then, F12K culture medium containing the Molego 1 (Molego 1 (30 µM) was dissolved in culture medium (including 1% DMSO, 1% Cremophor®EL)) was added and incubation for another 2 h. After that, the cells were washed with PBS for 3 times at room temperature, and then trypsinization and resuspended in culture medium, the cells concentration kept at 6.8×10⁶ cells/ml. Finally, the cells were transferred to a 10 mm NMR tube, and the Hyper-CEST spectra and MRI experiments were performed. For the control experiment, the cells were incubated with NEM for 2 h firstly, and the residual quantities of NEM not taken up by the cells were washed by PBS for 3 times. After that, the cells were incubated with Molego 1 for another 2 h. Other procedures were carried out similarly to the case of the experimental group. For the Hyper-CEST NMR experiment, the procedures were same to the Hyper-CEST NMR in solution, but the swept across the chemical shift range changed to 55-85 ppm in 1-ppm steps. For the Hyper-CEST MRI experiment, 16 off-resonant (119 ppm) and 16 on-resonant (-119 ppm) (The chemical shift of dissolved ¹²⁹Xe was set as 0 ppm) scans were acquired and averaged. The image was acquired using a RARE sequence (slice thickness=25 mm, matrix size=32×32, in-plane resolution=0.9375×0.9375 mm², FOV=30×30 mm², centric k-space encoding, bandwidth=5400 Hz, echo time=4.65 ms, repetition time=28077 ms, centric k-space encoding, no partial Fourier transform acceleration, rare factor=16). And the rest procedures were carried out same to the Hyper-CEST MRI in solution.

Tumor lysate Hyper-CEST spectra and MRI studies

After the A549 tumor model mice was injected with Molego 1 (1 mM, in 100 μ L of PBS solution, including 1% DMSO, 1% Cremophor®EL)) through intratumor injection. The tumor was resected after 3 h, and make of homogenate through homogenizing machine. 1 mL water was added into the tumor homogenate and centrifuge for 3 min at 3000 rpm, and the supernatant was obtained. And then, 200 μ L supernatant was diluted into 2 mL, and transferred to an NMR tube (10 mm), and the Hyper-CEST NMR/MRI were acquired. For the Hyper-CEST NMR experiment, the procedures were same to the cellular Hyper-CEST NMR. For the Hyper-CEST MRI experiment, 16 off-resonant (119 ppm) and 16 on-resonant (-119 ppm) (The chemical shift of dissolved 129 Xe was set as 0 ppm) scans were acquired and averaged. The image was acquired using a RARE sequence (slice thickness=25 mm, matrix size=32×32, in-plane resolution=0.9375×0.9375 mm², FOV=30×30 mm², centric k-space encoding, bandwidth=5400 Hz, echo time=4.65 ms, repetition time=33077 ms, centric k-space encoding, no partial Fourier transform acceleration, rare factor=16). And the rest procedures (except to the saturation pulse, in this experiment, a 13 μ T with 10 s saturation pulse was used) were carried out same to the Hyper-CEST MRI in solution.

Antitumor activity studies in vivo

The chemotherapy efficacy of Molego 1 was performed on flank A549 mouse tumor model. Tumor bearing mice were established by subcutaneous inoculation of A549 cell suspension (2×10^6 cells per mouse) into the right flank region of 5-week BALB/c male mice, respectively. When tumors reached 150-200 mm³, all mice were randomly divided into three groups with four mice in each group: (1) PBS control, (2) CRB and (3) Molego 1. The doses of CRB, and Molego 1 were fixed at 10 μ mol/kg body weight. Molego 1 or CRB was dissolved in DMSO, and then stock in PBS (including 1% DMSO, 1% Cremophor®EL) and injected in tumor directly every 3 days and 5 times total. The tumor size was measured with a digital caliper every 3 days before treatment. Tumor volumes were calculated as follows: tumor volume (mm³) =(width² x length)/2. Relative tumor volumes were calculated as V/V₀; V₀ was the initial tumor volume at the start of the treatment. Finally, on the 15th day, blood samples were drawn from the eyeball of the above mice in each group for hematology analysis. All of the mice were sacrificed and tumors were collected from each group for photographed. The tumors were excised for hematoxylin and eosin (H&E)





stain, TUNEL stain for histopathological analysis. And the heart, liver, lung, spleen, and kidney were excised for H&E stain for histopathological analysis.

QUANTIFICATION AND STATISTICAL ANALYSIS

Quantification and statistical analysis of CEST and fluorescence *in vivo* were performed by Origin version 2016 for Windows (Origin Software, USA), all results are expressed as mean \pm SD as indicated. The MR images were processed on MATLAB (R2014a, MathWorks, Natick, MA). And the details can be found in STAR Methods.